# SimRadar: A Polarimetric Radar Time-Series Simulator for Tornadic Debris Studies

Boon Leng Cheong, David J. Bodine, Caleb J. Fulton, *Senior Member, IEEE*, Sebastián M. Torres, *Senior Member, IEEE*, Takashi Maruyama, and Robert D. Palmer, *Fellow, IEEE* 

Abstract—In an effort to study and characterize scattering mechanisms of debris particles in tornadoes, a numerical polarimetric radar emulator was developed. This paper is primarily motivated by attempts to explain radar observations near tornadoes. One such observation is the regions of negative differential reflectivity, which have been found near tornadoes but they are yet to be explained physically. There are hypotheses that suggest common debris alignment and/or dominant scattering from objects with high radar-cross-section (RCS) values that cause negative  $Z_{DR}$ , but they are extremely challenging to verify due to the inherent danger near the vicinity of tornadoes. It is, however, possible to numerically construct the scenes through representative simulations to verify the plausible causes. This serves as our primary motivation to develop the radar emulator. The novel aspects of this paper are the realistic trajectory derivation, which is based on a physical air-drag model, and the representative diversity of RCS contributions from each debris object, developed through realistic polarimetric RCS modeling and anechoic chamber measurements.

Index Terms—Polarimetric radar, radar cross section, simulation, software, time series.

#### I. Introduction

TORNADOES are undoubtedly one of the most dangerous natural disasters. Knowledge of their location and trajectory is essential to forecasters and emergency meteorologists to assess the affected areas and issue warnings to the general public in order to let them have sufficient time to take shelter. In the United States, the nationwide network of the WSR-88D (Weather Surveillance Radar 1988 Doppler) is the key instrument to observe severe weather, including tornadoes. Radar products are used to predict weather and issue warnings such as tornado trajectories [1]. With the recent upgrade to include

Manuscript received August 23, 2016; revised December 2, 2016; accepted January 6, 2017. Date of publication February 17, 2017; date of current version March 17, 2017. This work was supported by the National Science Foundation under Grant AGS-1303685.

- B. L. Cheong and D. J. Bodine are with the Advanced Radar Research Center, University of Oklahoma, Norman, OK 73019 USA (e-mail: boonleng@ou.edu).
- C. J. Fulton is with the School of Electrical and Computer Engineering, University of Oklahoma, Norman, OK 73019 USA.
- S. M. Torres is with the School of Electrical and Computer Engineering, University of Oklahoma, Norman, OK 73019 USA, and also with the National Severe Storms Laboratory, National Oceanic and Atmospheric Administration, Norman, OK 73019 USA.
- T. Maruyama is with the Disaster Prevention Research Institute, Kyoto University, Kyoto 611-0011, Japan.
- R. D. Palmer is with the School of Electrical and Computer Engineering, University of Oklahoma, Norman, OK 73019 USA, and also with the School of Meteorology, University of Oklahoma, Norman, OK 73019 USA.

Color versions of one or more of the figures in this paper are available online at http://ieeexplore.ieee.org.

Digital Object Identifier 10.1109/TGRS.2017.2655363

dual-polarization capabilities [2], new polarimetric variables allow for a new signature, known as the tornado debris signature (TDS), to be derived. The TDS is a combination of high reflectivity factor (Z > 45 dBZ), low copolar cross-correlation coefficient ( $\rho_{HV} < 0.8$ ), and low differential reflectivity values (ZDR < 0.5 dB) [3]. It is emphasized here that the TDS corresponds to a tornado that has already caused damage, i.e., it indicates the presence of debris in the air. Nonetheless, the TDS can help estimate the severity of damage caused by tornadoes [4], [5].

One other signature that often (not always) appears alongside the TDS is regions of negative differential reflectivity  $(Z_{DR})$ . Since the dual-polarization upgrades, this signature has been observed, but there is no definitive physical explanation to help us understand the underlying phenomena. While debris have been observed to tumble randomly, the negative  $Z_{DR}$  suggests otherwise. One hypothesis suggests common alignment [6], [7], which means a general preference toward vertical orientation of debris objects near the tornado vortex. The common alignment may be due to centrifuging effects of debris. With the bulk of debris being oriented vertically, this results in an average negative  $Z_{DR}$  measured by a radar. While the hypothesis is plausible, the inherent danger near a tornado prohibits in situ measurements to be obtained. Needless to mention that capturing the 3-D orientation of an object is in itself a very challenging task. Therefore, this paper describes a method to computationally construct the scene for radar data. Using the standard radar processing methods to produce radar products, similar signatures can later be identified for their true underlying physical constructs. In order to correctly construct the physical scene, two key ingredients must be modeled accurately: the trajectory of motion and the radar cross section (RCS) of tornadic debris particles. These are the novel aspects of this paper.

Numerical derivation of time-series data that exhibit the same characteristics as weather radar signals has been introduced since the early work documented in [8], which utilizes a random number generator to produce weatherlike signals with a desired spectrum shape, often a Gaussian function. The method does not incorporate any weather physics, but it still serves as a useful tool to study signal processing methods, even today. Since then, a few other advanced radar simulators that produce time-series data were developed. Some significant ones were documented in [9]–[12]. The work in [9] uses a collection of point targets to synthesize backscattered signals from the atmosphere. The work in [10] is an extension

of [8] that can efficiently simulate signals from horizontal and vertical polarizations. The signals can have any desired specific phase and cross correlation coefficient chosen by the user. In [11], individual rain drops are emulated to produce timeseries data from a radar volume. The work was extended to include polarimetric capability, which was documented in [12]. Due to the computational requirements, these methods are limited to a single radar volume.

To study the regions of negative  $Z_{DR}$ , a collection of multiple radar volumes is necessary in order to encapsulate the entire area that contains the vortex core, the debris particles that are carried around by the wind field, and some areas outside of the tornado where debris ejections occur. A previously developed physically based radar simulator is capable of producing time-series data from a swath composed of multiple radar cells in both range and azimuth [13]. The framework ingests weather background produced by a separate numerical model. This approach loosens the coupling between the radar time-series emulation and the physical weather modeling. The work was later expanded to incorporate polarimetric capabilities [14] and recently adopted for phased array simulation [15].

Based on the work from [13] and [16], the simulation concept has been expanded to include debris particles. The simulation has been restructured to take advantage of graphic processing unit parallel computing. In this paper, the motions of the debris particles are derived based on trajectory calculations developed in [17], which are based on air drag and angular momentums caused by the impinging wind. These parameters are obtained by wind tunnel measurements at Kyoto University. The RCS values of the debris particles at any given orientation from the perspective of the radar are either computed in real time or looked up from a tabularized database (for complex objects), which was developed through finite-element simulations and validated by anechoic chamber measurements. In this paper, an overview of the new simulation framework will be provided. The key ingredients, airdrag model (ADM) and RCS, will be described in detail. Then, limited simulated time-series data, their spectra, and radar products will be presented to illustrate the potential of this framework. Finally, some possible future work will be discussed.

## II. SIMULATION FRAMEWORK OVERVIEW

The emulation of volume scattering is accomplished through a coherent sum of a large number of individual point scatterers, similar to the *Monte Carlo* method. These point scatterers are also known as the scattering centers or the sampling positions of a volume. With a sufficiently large number of these point scatterers, the coherent integration of the backscattered signals from these points resembles the return signal from distributed targets.

Each particle has polarimetric amplitudes that are weighted based on its position relative to the scan range and antenna pointing direction. Mathematically, the mechanism can be represented by

$$x[n] = \sum_{i=1}^{N} A^{(i)} \exp\left(-j\frac{4\pi r^{(i)}}{\lambda}\right) \tag{1}$$

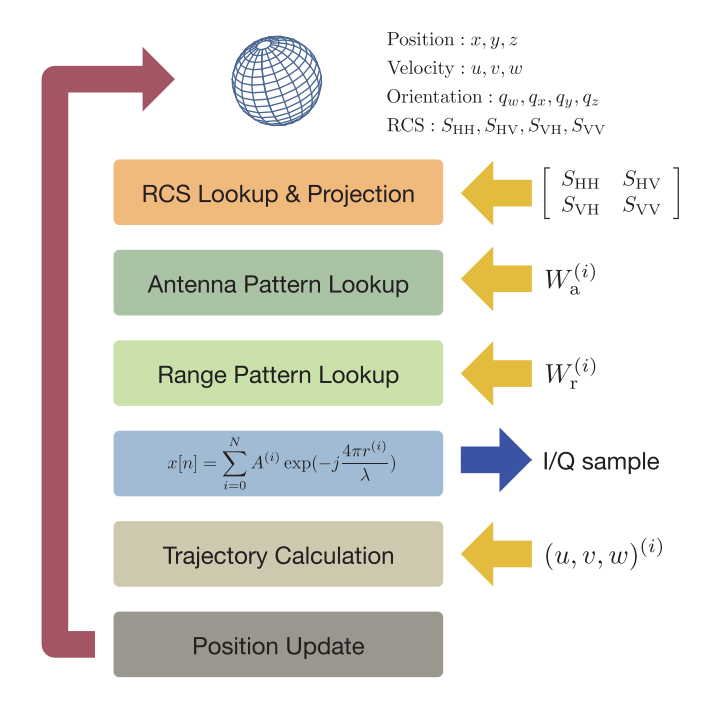


Fig. 1. Flowchart of radar signal emulation during each pulse cycle.

where  $A^{(i)}$  represents the amplitude of the signal backscattered by the ith point scatterer (for debris) or scattering center (for hydrometeors) including antenna pattern and range-weighting function effects,  $r^{(i)}$  represents its range,  $\lambda$  is the system wavelength, and N is the total number of point scatterers in the emulation domain. In this simulation framework, (1) is carried out for each of the four polarimetric backscattering components (copolar horizontal and vertical and the two crosspolar terms).

Fig. 1 shows the process to compute a radar sample, which is repeated K times to obtain K samples. Each point scatterer has a set of attributes, i.e., position, velocity, orientation, rotational speed (change of orientation), drag coefficients, RCS, and house-keeping parameters, such as identification tag, size, mass, and so on. Many of these parameters change with time. For example, the position changes based on the background velocity, its present velocity, and air drag as a function of orientation. Another example is the orientation, which changes based on its present velocity, the background velocity, and its angular momentum as a function of its orientation. These aspects will be discussed in more detail in Section II-C. If a scatterer exits the simulation bounds (from the position update), it is replaced by a new scatterer in which the position is set randomly within the domain for meteorological targets (rain drops) but near the ground for tornadic debris.

The amplitude  $A^{(i)}$  in (1) can be broken down further into

$$A^{(i)} = \left(\frac{1}{r^{(i)}}\right)^4 Z^{(i)} W_{\mathbf{a}}^{(i)} W_{\mathbf{r}}^{(i)} \tag{2}$$

where  $r^{(i)}$  represents the range of the point scatterer or scattering center,  $Z^{(i)}$  represents its intrinsic reflectivity,  $W_{\rm a}^{(i)}$  represents the weight due to the antenna pattern, and  $W_{\rm r}^{(i)}$  represents the weight due to the range-weighting function, which is mainly attributed to the transmit waveform,

subsequent matched-filtering, and receiver impulse response. After summing contributions from each point scatterer, the individual velocities are updated based on each target's trajectory. This process is described next.

For the hydrometeors, depending on the position of the scatterer relative to the weather data cube (table), velocity is obtained through table lookup and trilinear interpolation in space (more on velocity parameterization in Section II-F). The same table is used until the next time step. That is, the velocity of a point scatterer depends only on its position within the table. Interpolation of the velocity vector in time is avoided without sacrificing realism, as it would *blur* the values between two tables and reduce the spatial structure of the data cube.

For the tornadic debris, velocity is updated based on the background wind field and the ADM of the object. An object can be initialized with zero velocity on the ground, letting the background wind slowly introduce nonzero velocity to the object, much like how debris objects are actually carried aloft by tornadoes.

#### A. Coordinate System

A Cartesian world coordinate system is used to describe the x, y, and z components of position and velocity of a scatterer. For hydrometeors, there is no need to describe their orientation due to their inherent symmetry. For debris objects, a unit quaternion is used to describe their orientation. Local angles of the wind vector impinging the object, denoted as  $\alpha$  and  $\beta$ , are calculated based on the local x-, y-, and z-axes, which are the functions of the orientation quaternion. Similarly, local angles of the electromagnetic wave impinging the object, denoted as  $\theta$ ,  $\phi$ , and  $\psi$ , are calculated based on another local x-, y-, and z-axes, which are separate functions of the orientation quaternion. These will be discussed in more detail in the following Sections B, C and D.

## B. LES Model

The framework utilizes tornadic wind fields produced by a large Eddy simulation (LES) model to drive the motions and orientations of debris and hydrometeors. Briefly, it is a fluid dynamic model that uses a shallow region of inflow with a specified angular momentum. The updraft at the top of the domain drives a swirling flow that converges at the central axis to form a tornado. The numerical model uses a stretched grid with horizontal and vertical grid resolutions up to 3 m in the center of the tornado. The reader is referred to [18]–[20] for detailed information on the LES numerical simulation.

The present simulation framework supports both uniformly and exponentially gridded data cubes. The exponentially gridded data cube is used to provide maximum resolution near the ground, at the center of the simulation domain where drastic changes occur. Various configurations such as two-cell or multiple subvortices have been incorporated into the framework.

### C. Trajectory Calculation

The ADM of both meteorological and debris scatterers is physically based. Trajectories and orientations are computed

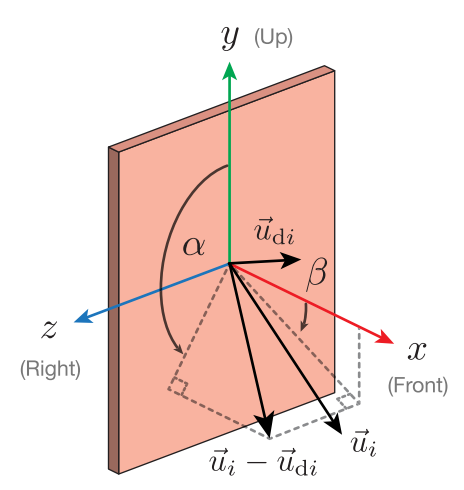


Fig. 2. Background wind vector  $\vec{u}_i$  and the debris object. The coefficients of air drag  $\vec{c}_D$  and angular momentum  $\vec{c}_M$  are functions of the object's velocity  $\vec{u}_{di}$ , the background velocity  $\vec{u}_i$ , and its orientation with respect to its local x-, y-, and z-axes. The angles  $\alpha$  and  $\beta$  are used in the ADM table lookup.

using wind vectors at the position of the scatterer in the LES datacube. Debris trajectories for small, nearly spherical particles, e.g., rain drops or dust, are computed using the methodology outlined in [19]. Nonspherical scatterers have been observed to tumble in tornadoes and, therefore, their rotational characteristics are described as a function of the background wind speeds and physical debris properties. To more realistically simulate both the trajectories and orientations of nonspherical scatterers, a six degree-of-freedom (6DOF) model is implemented [21], [22]. The 6DOF model calculation employs drag force and moment coefficients from wind tunnel measurements at a wind tunnel facility operated by Kyoto University.

A local coordinate system to represent the wind flow with respect to the object of interest is introduced here. Fig. 2 shows an object at its reference frame and a vector representing the background wind vector impinging the object  $(\vec{u}_i)$ . The local x-, y-, and z-axes are simply the rotation of the cardinal x-, y-, and z-axes (vectors) by the unit quaternion of the object. The geometrical representations of  $\alpha$  and  $\beta$  are also shown. These angles are used to lookup an entry of drag and angular momentum coefficients  $(c_{D,x}, c_{D,y}, c_{D,z}, c_{M,x}, c_{M,y},$  and  $c_{M,x})$ .

At each time step, the velocity (vector) of the *i*th debris object, denoted as  $\vec{u}_{di}$ , is updated according to

$$\frac{\partial \vec{u}_{di}}{\partial t} = T_a ||\vec{u}_i - \vec{u}_{di}||^2 \vec{c}_D(\vec{u}_i - \vec{u}_{di}, \alpha, \beta) + \vec{g}$$
 (3)

where  $T_a$  represents the Tachikawa parameter [17],  $\vec{u}_i$  represents the meteorological background wind vector from the LES model,  $\vec{c}_D$  represents the drag force coefficient,  $\alpha$  and  $\beta$  represent the displacement angles of the wind vector relative to the reference frame of the debris piece, and  $\vec{g}$  represents the acceleration due to gravity. The arguments of  $\vec{c}_D$ , i.e.,  $\vec{u}_i - \vec{u}_{di}$ ,  $\alpha$ , and  $\beta$ , indicate that the drag coefficient is a function of the difference between an object's present velocity and the background velocity, which provide the relative impinging wind magnitude and orientation, described by  $\alpha$  and  $\beta$ , which can be derived using geometry.

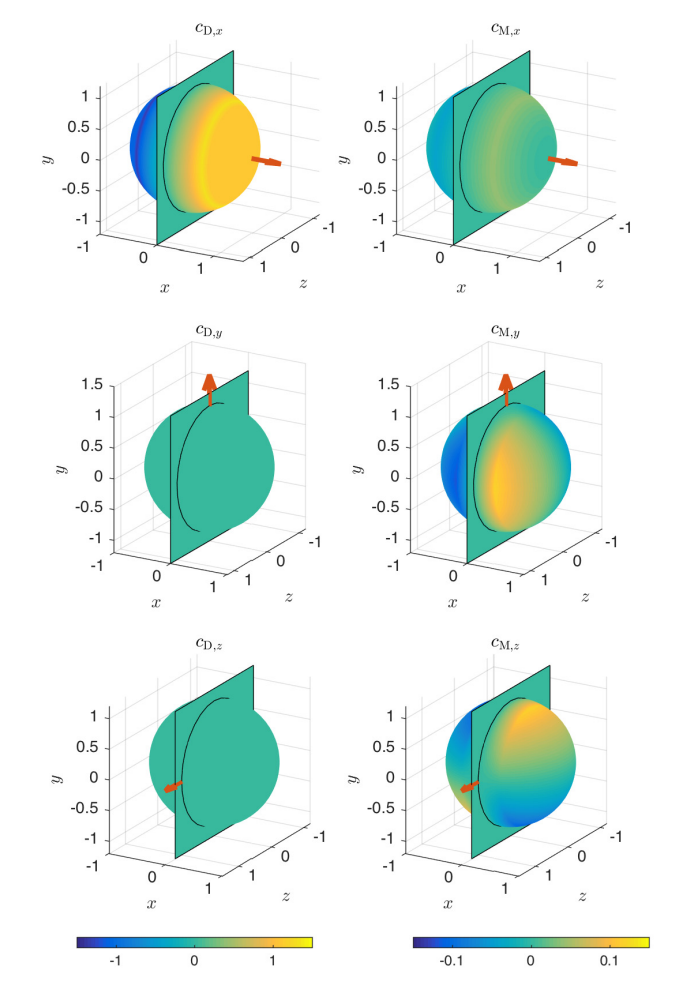


Fig. 3. Measured drag and angular moment coefficients of a square plate.

Similarly, the rotational velocity of the debris object, denoted as  $\vec{\omega}_{di}$ , is calculated using

$$\frac{\partial \vec{\omega}_{di}}{\partial t} = T_a ||u_i - u_{di}||^2 \vec{c}_M(u_i - u_{di}, \alpha, \beta) \tag{4}$$

where  $\vec{c}_M$  represents the angular moment coefficients.

The orientation of an object is represented by a unit quaternion. Compared with Euler angles, it avoids the problem of gimbal lock. Quaternion arithmetic is somewhat similar to matrix arithmetic but different. The reader is referred to [23] for more information. Once the rotational velocity is calculated, the orientation of the scatterer is updated using a quaternion multiplication as follows:

$$\vec{q}_{k+1} = \vec{p}\vec{q}_k \, \vec{p}^{-1} \tag{5}$$

where  $\vec{p}$  is the composite rotation described by the x, y, and z elements in (4), which can be mathematically described as

$$\vec{p} = \vec{p}_x \vec{p}_y \vec{p}_z \tag{6}$$

where  $\vec{p}_x$ ,  $\vec{p}_y$ , and  $\vec{p}_z$  represent the unit quaternions of rotation about the x-, y-, and z-axes, respectively. In practice, extra care is taken to maintain the unity magnitude of  $\vec{q}_{k+1}$  so that it can properly represent an orientation, i.e., rotation from its initial state. Fig. 3 shows an example of measured drag and angular momentum coefficients of a square plate.

#### D. Radar Cross Section of Debris

The RCS table of an object contains three components: copolar complex amplitude  $S_{HH}$ , copolar vertical complex amplitude  $S_{VV}$ , and cross-polar complex amplitudes  $S_{HV} = S_{VH}$ . They are generated offline, outside of the simulator, through several methods that will be discussed later, and stored in a predefined format for efficient table lookup in the simulator. Fig. 4 shows an example RCS of a thin sheet with a cylindrical stem, which can be used to represent a leaf. Leaves will be used to represent tornadic debris in the rest of this paper.

Fig. 5 shows the geometry representation of  $\theta$ ,  $\phi$ , and  $\psi$ . During the simulation session, at a given antenna pointing direction, two incident angles of the electromagnetic wave and a roll angle are first computed. Then, they are used to look up and derive the return signals of the horizontal and vertical polarizations. The incident angles,  $\theta$  and  $\phi$ , are akin to the longitude and latitude angles used to described any position on the Earth. Once the appropriate RCS values of the co- and cross-polar components are found, the roll angle,  $\psi$ , i.e., how an object is rotated about the radar beam vector, is used to compute the new H and V components of the object through a polarization basis transformation. In this paper, a catalog library of RCS has been built with  $\theta$  and  $\phi$  stored in an incremental grid of 5°. Such spacing was found to be sufficient for the leaves, but not generally. A linear interpolation scheme is applied during the lookup process.

Electrically small, spherical objects (sand and dust particles) are modeled as spheroids using the T-matrix method [24]. This is also used for more flat (but still spheroidal) objects near the Mie scattering regime. For straight, mostly cylindrical, and high-aspect-ratio scatterers, a truncated cylinder formulation based on [25] is used with the addition of endcap scattering based on physical optics (PO) for objects with electrically large diameters. Currently, twigs, bare/straight branches, iron rods, and so on fall into this category. These, in general, contribute both specular flashes and depolarizing effects. For objects that are mostly flat, rectangular, and are either lossy and of moderate to large electrical size or are highly reflective/conductive and electrically large, the PO is again used, based on the formulation in [26]. Both the flat sheet and cylindrical formulations operate by "truncating" equivalent surface currents derived from infinite geometries to finite dimensions, using reflection coefficients (flat sheet) or modal expansions (cylindrical) of the infinite geometries. This is done for both TE and TM polarizations, followed by careful transformations to the local bases. These do not take into account edge diffraction [27], which is why this technique is currently limited to flat sheets that are either large or resistive, such as most leaves [26]. Currently, roof shingles, flat siding, structural steel/aluminum plates, drywall, foam insulation, and other such building materials fall into this category. Combinations of these techniques are being used for leaves. The example in Fig. 4 is modeled as a thin resistive sheet with a cylindrical dielectric stem, using material properties from [26]. Both the specular flashing from the sheet and significant polarization-dependence from the stem are exhibited.

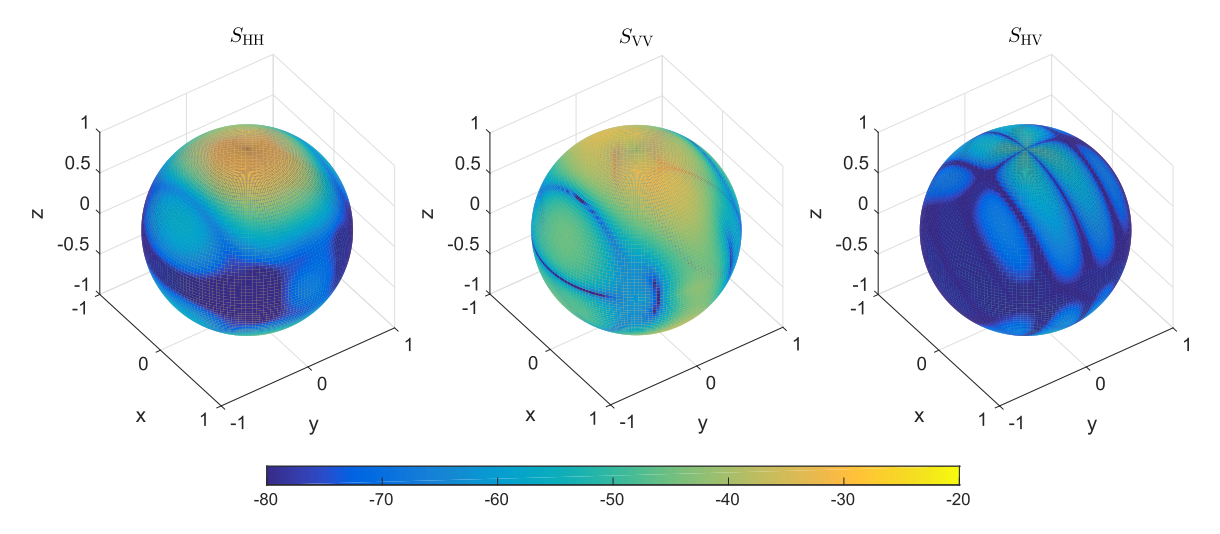


Fig. 4. Example far-field RCS of a simulated leaf, which contains the copolar amplitude of H polarization  $S_{HH}$  (left), the copolar amplitude of V polarization  $S_{VV}$  (middle), and cross-polar amplitude  $S_{HV}$  (right). The leaf is simulated as a resistive sheet with a stem (cylinder) (width = 6 cm, height = 8 cm, thickness = 0.2 mm, stem length = 12 mm, stem diameter = 1.5 mm, and moisture content = 80%) at 2.8 GHz.

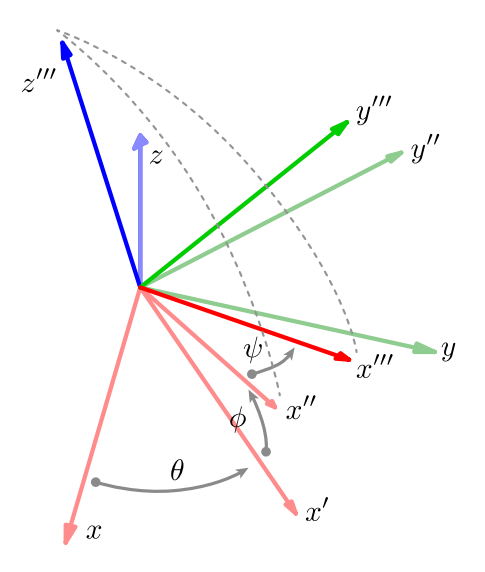


Fig. 5. RCS coordinate system based on the 3-2-3 convention. The radar look direction is always from the z-direction (top looking down). Any position on an RCS table (a spherical surface of Fig. 4) can be described by rotation of  $\theta$  about the z-axis, then  $\phi$  about the y'-axis (y' = y"). The third angle  $\psi$ , which is the rotation about the z'''-axis, is used to derive the appropriate RCS components through a polarization basis transformation.

In addition to dividing objects into different sizes to capture their primary scattering behaviors, we have also considered generating the RCS of simple objects in real time. For example, the RCS of a twig, of length on the orders of tens of  $\lambda$ , can be modeled sufficiently accurate using a long and thin cylinder. It can be derived analytically at a low computational cost, sometimes less than the procedure of table lookup and linear interpolation. Such simple objects can be made to form a rich population of size variations, allowing the simulation of rich collection of debris within a cloud. The following discussion summarizes the different approaches currently being taken for different object types.

For complex debris objects for which the RCS cannot be modeled analytically and efficiently, the RCS tables are obtained through finite-element simulations in Ansys HFSS; for simple objects, these simulations are validated by measurements in an anechoic chamber, which are always validated with calibration spheres. The material properties for simulation and computational techniques are verified with network analyzer-based measurements [28]. As mentioned earlier, the angular steps,  $\Delta\theta$  and  $\Delta\phi$ , are chosen to be 5°. From our experience through trial and error, this step size along with linear interpolation is sufficient to maintain the fidelity needed to emulate the electromagnetic characteristics of most debris types in the radar simulator. The expansion of the library to cover more objects at S- and X-bands for the smaller/simpler objects considered will be a continuing effort as we explore different scientific objectives in the future.

## E. Visualization

A significant amount of effort was devoted into developing a visualization tool for the radar simulator. It is extremely valuable during the development of debris motion and orientation. Fig. 6 shows an example screenshot of the graphical user interface (GUI) of the simulator, with a tornadic vortex occupying a volume of approximately  $1.1 \times 1.1 \times 1.1 \text{ km}^3$ . On the main view, the rain drops within the tornadic vortex shown in purple can be seen. The scatterers are drawn with the color table shown at the bottom, with their opacity set as a function of drop size, much like higher return power is expected from larger drops. This visualization shows that the scatterers centrifuge around the regions where the wind velocity is highest, i.e., a funnel shape. The green particles represent debris. In this example, a debris population of 10<sup>5</sup> leaves is used, and as one would expect, most debris particles concentrate at the bottom of the domain. The top right subview shows the debris particles from the perspective of the radar. This GUI is interactive, allowing us to pan, tilt, and zoom to visualize the scatterers and debris particles within the domain. Several draw modes are also available to view the simulation domain, one of which is to color the particles with their  $Z_{DR}$  values, which will be presented later.

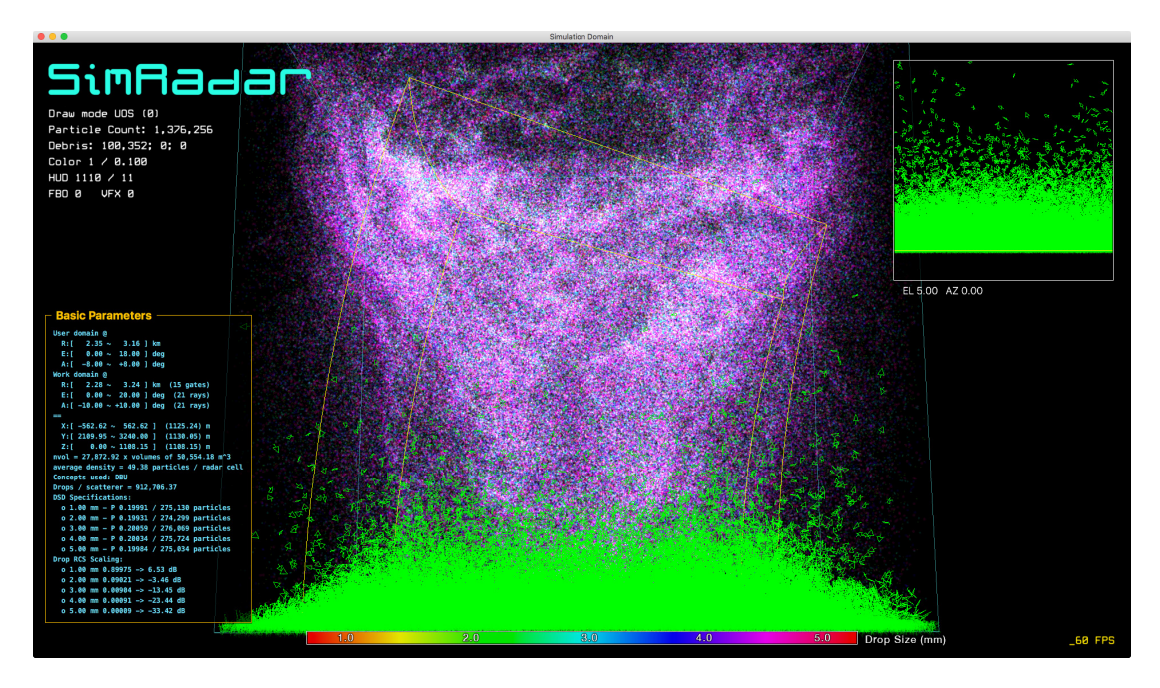


Fig. 6. GUI of SimRadar is an interactive view that allows us to pan, tilt, and zoom around the domain in order to visually inspect the simulation configurations and validate the proper implementation of various components of the simulator. On the main view, rain drops within a tornadic vortex are shown in purple region; the debris objects are shown in green region. As one would expect, most of them are concentrated near the ground. A subview on the upper right shows the debris objects from the perspective of the radar.

## F. Parameterizations and Modes of Operations

Some scenarios require simplifying the simulation configurations in order to identify specific contributions from a particular variable. For instance, one may want to study the behaviors of big drops near a tornado alone. In this case, a custom DSD with only one dropsize may be used. For another example, one may want to study the general orientation or concentration distribution of one debris type under a steady circulation. In this case, only one type of debris may be used.

In order to support a variety of range-weighting functions and antenna patterns, these weighting functions are implemented as a table lookup with linear interpolation. For example, one could set the range weighting to include sidelobe leakage to emulate what a pulse compression radar would observe. As another example, one could set the transmit antenna pattern to be wide and simulate multiple receivers for beamforming studies.

The simulation framework has been implemented to support a couple of different modes of operation. One such mode is that the hydrometeors are being dragged (3), which would otherwise be assigned with the velocity of the background wind field, playing the role of background wind tracers. On the other hand, when the scatterers are being dragged by the background wind, they experience individual acceleration by the background air drag and gravity. This mode of operation allows for the study of debris centrifuging and/or size sorting around to the tornado vortex, for example.

The other mode of operation is by scaling the return signals of each scatterer in order to represent an arbitrary DSD profile with a uniform counterpart. Because of the exponential nature of any representative DSD, either Marshall–Palmer (MP) [29] or other variants of gamma DSDs [30], [31], [32], the number

of large drops is extremely low, which results in a low number of scatterers that represent large drops. This causes an undesired artifact where a scatterer that represents numerous big drops does not break up. Instead, as it moves, it represents a clump of big drops that move together, which ultimately shows up as a hot spot in radar reflectivity map. This is not realistic and must be handled differently. One way to deal with this is by using an extremely large number of scatterers, which would require an even larger number of small drops in order to represent the selected DSD, resulting in a significant computational expense. The other method would be to uniformly redistribute the scatterers across all drop sizes and then later adjust the return signals from each scatterer to compensate for the population ratio adjustments through a scaling factor. This method will be referred to as the scaled reflection (SR) model, which was introduced in the work of [20] and adopted here as one of the modes of operation.

Fig. 7 shows a set of simulations using these two different modes of operations to illustrate the clumping effects and the adopted SR solution to mitigate the unrealistic outcomes. Each row shows a radar image, a sequence of time-series samples (I/Q components and its amplitude A), and the corresponding spectrum from a selected radar cell. The data on the first row are obtained from the legacy mode of operation where each raindrop is represented by one scatterer. This setup is what we consider the reference emulation as the raindrop population is emulated in a one-to-one manner, i.e., one scatterer to represent one rain drop. The simulation was configured with the parameters listed in Table I. To be fair, the selection of DSD profile, drop size and drop count can be a complex procedure if one would like to finely tune the precipitation parameters of the background; the emulator framework presented here is

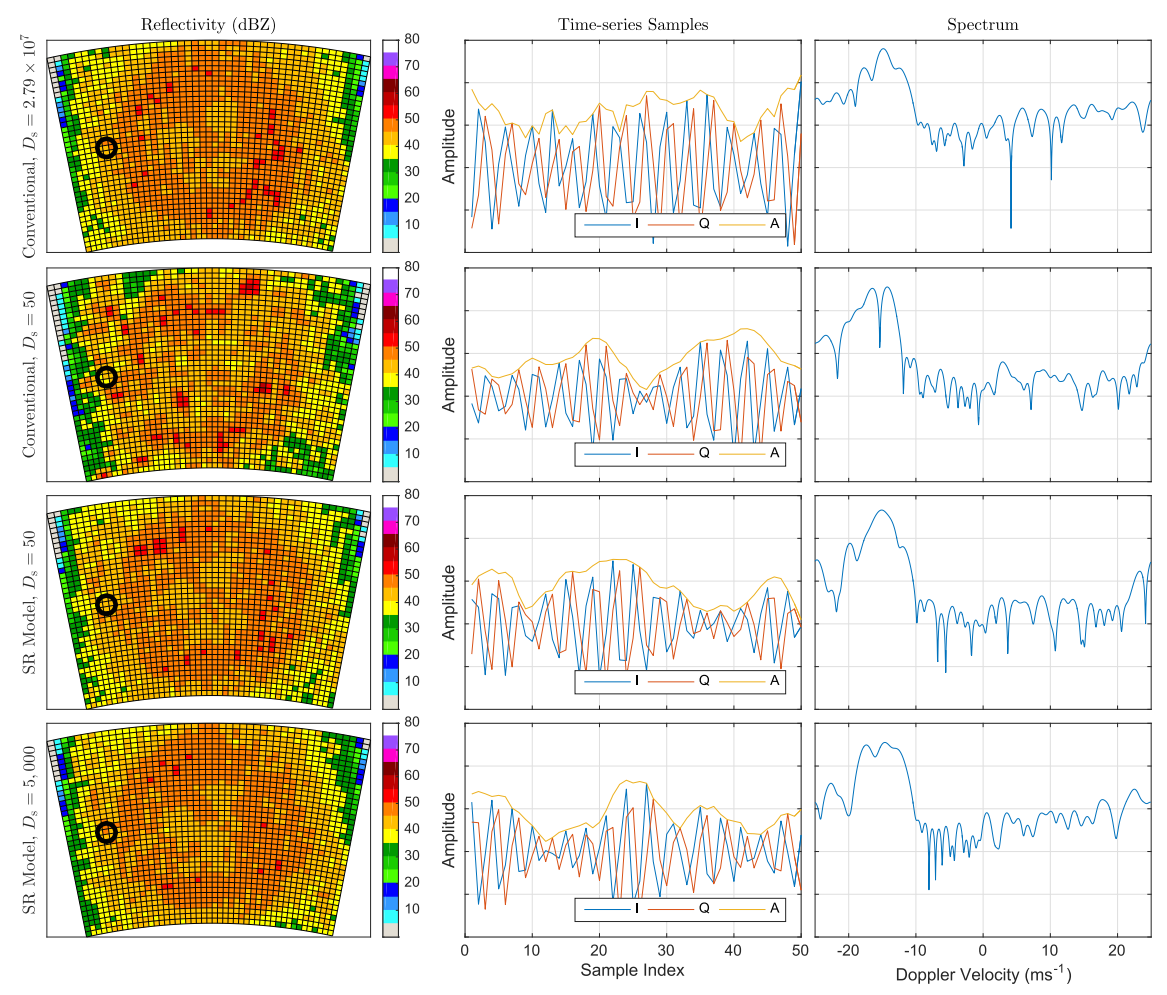


Fig. 7. Comparisons between the accurate and the simplified models. Without using the SR model, the scatterer density  $D_s$  required is  $2.79 \times 10^7$  (unitless, number of scatterers per resolution volume) for this setup, which is computationally extremely expensive. This reference case took two months to complete. In general, all simulations resulted in similar time-series data, with no significant differences in their corresponding spectra. The legacy model with  $D_s = 50$  (second panel) is clearly not suitable for modeling even a simple DSD with five drop sizes, producing hotspots in the reflectivity map. The uniformly redistributed DSD with scaled reflection (third and fourth panels) is much closer to the reference. With the SR model,  $D_s = 50$  is sufficient and, from our experience, higher densities do not produce any significant improvements.

TABLE I

PARAMETERS TO GENERATE A REFERENCE SETUP WHERE EVERY
RAIN DROP IS EMULATED WITH A DISCRETE SCATTERER

| Parameters             | Values  |
|------------------------|---|
| Radar wavelength       | $0.10{ m m}$  |
| Radar beamwidth (3-dB) | 1.0°  |
| Radar beam pattern     | $\frac{8J_2[(\pi D\sin\theta)/\lambda]}{[(\pi D\sin\theta)/\lambda]^2}$ |
| Scan elevation         | 3.0°  |
| Range gate spacing     | $30\mathrm{m}$  |
| Pulse repetition time  | $5 \times 10^{-4}  \text{s}$  |
| Drop concentration     | $870 \text{ m}^{-3}$  |
| MP DSD profile         | $8.0 \times 10^6 e^{-2.3D} \mathrm{m}^{-3} \mathrm{mm}^{-1}$            |
| Drop sizes             | $1, 2, 3, 4, 5 \mathrm{mm}$   |
| Plate size             | $0.04\mathrm{m} \times 0.04\mathrm{m} \times 0.002\mathrm{m}$           |
| Plate density          | $1120  {\rm kg}  {\rm m}^{-3}$  |

capable of this. Nonetheless, for the purpose of demonstrating the efficacy of using the SR model, the proposed simple DSD is sufficient. The drop density is consistent with what has been commonly measured by disdrometers [33], [34]. What we look for is to produce radar images and time-series samples that are statistically invariant.

As expected, the time-series samples are of typical characteristics, showing slow oscillations that indicate nonzero

velocity, and their power spectrum density has a Gaussian shape. The second row of Fig. 7 shows the result with "hotspots," which was generated using a low scatterer density  $D_s = 50$ . It is clear that this scatterer density is not sufficient when we have a population of scatterers with different reflectivity values within a resolution volume. This scenario is distinctively different from our previous work in [13] where all the scatterers within a resolution volume share the same reflectivity value. The third and fourth rows show the simulation result using the SR model, with  $D_s = 50$  (unitless, number of scatterers per resolution volume) and  $D_s = 5000$ , respectively. It is evident that the hotspots have been eliminated and a higher number of scatterers do not contribute significantly toward the radar reflectivity image or the I/Q time-series samples. Discussions to address the fine-tuning of  $D_s$  is presented next.

#### G. Scatterer Density

The scatterer density  $D_s$  is a key parameter that must be set correctly in order to achieve the volumetric scattering to properly emulate the meteorological background. In the

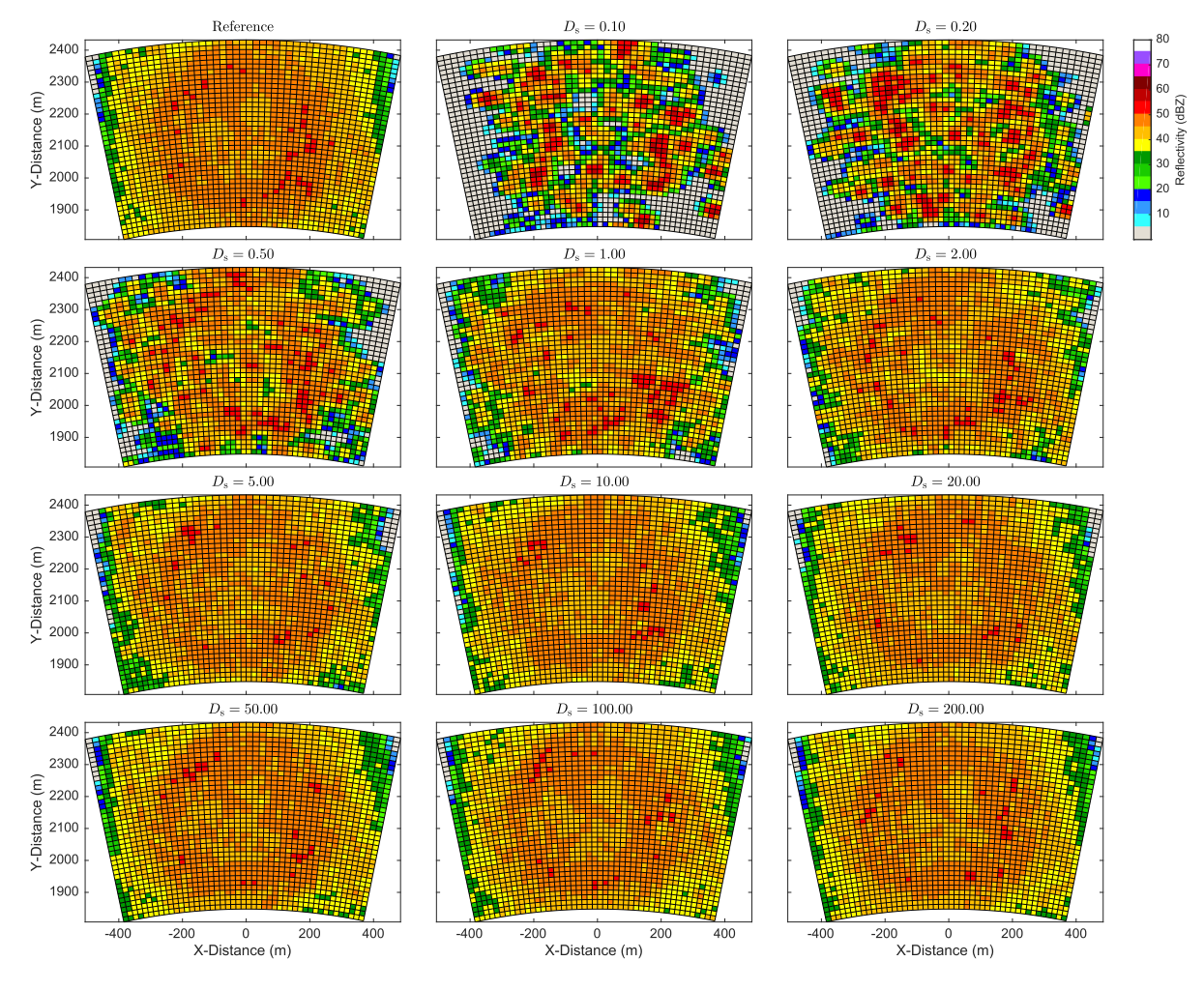


Fig. 8. Reflectivity fields generated using different  $D_S$  (unitless, number of scatterers per resolution volume). It is clear that individual scatterers unrealistically dominate the returns at different locations when  $D_S$  is low. At  $D_S < 1$ , which is less than one scatterer per range resolution volume, we could expect the radar to resolve them spatially. As  $D_S$  increases beyond 10, the return signals approach volumetric scattering just like a weather radar. No appreciable differences can be seen for  $D_S > 50$ , but a more quantitative analysis will follow in the text and in Fig. 9.

Section F, it was shown that the hotspot artifact can be eliminated using the SR model with a sufficiently large  $D_s$ . We suggest using  $D_s = 100$ . Fig. 8 shows a collection of radar reflectivity outputs using different  $D_s$  values. The reference reflectivity map that is shown in Fig. 8 is identical to the one in Fig. 7, which was shown earlier. At low  $D_s$ , a volumetric signal cannot be produced as there is less than one scatterer per resolution volume, i.e., the radar is capable of resolving individual point scatterers. Volumetric scattering starts to appear at  $D_s \approx 10.0$ , with no appreciable differences in reflectivity maps using higher  $D_s$ .

To more quantitatively assess the similarity to the reference case, a root mean square (rms) difference between each reflectivity map and the reference is computed and shown in Fig. 9. In addition, we also evaluated therms difference between Doppler velocity  $v_r$  and differential reflectivity  $Z_{DR}$ . As expected, one can see that all radar products converge toward the reference as  $D_s$  increases. Therms difference stabilizes right around  $D_s = 100$  and, thus, we propose to use this scatterer density with the SR model to properly emulate the meteorological background.

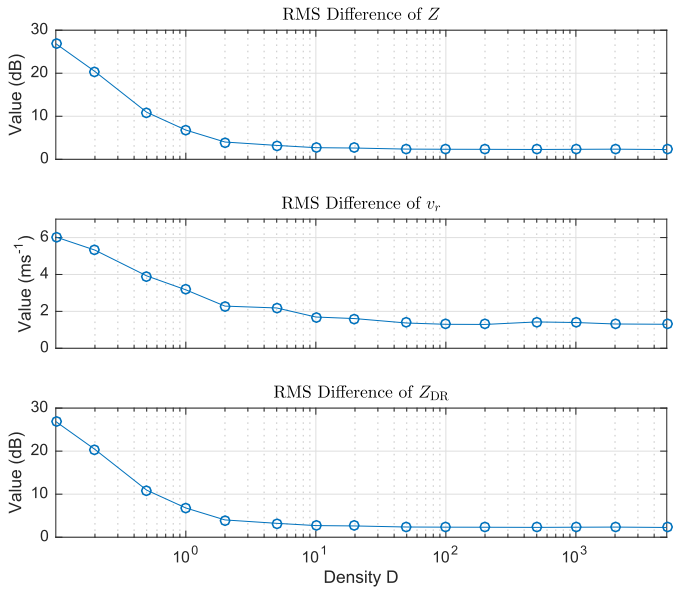


Fig. 9. RMS differences of Z,  $v_r$ , and  $Z_{DR}$  can be seen to decrease and taper off as  $D_s$  approaches  $10^2$ . No significant improvements can be seen after that, so we suggest using  $D_s = 100$  for the emulation of meteorological background using the SR model.

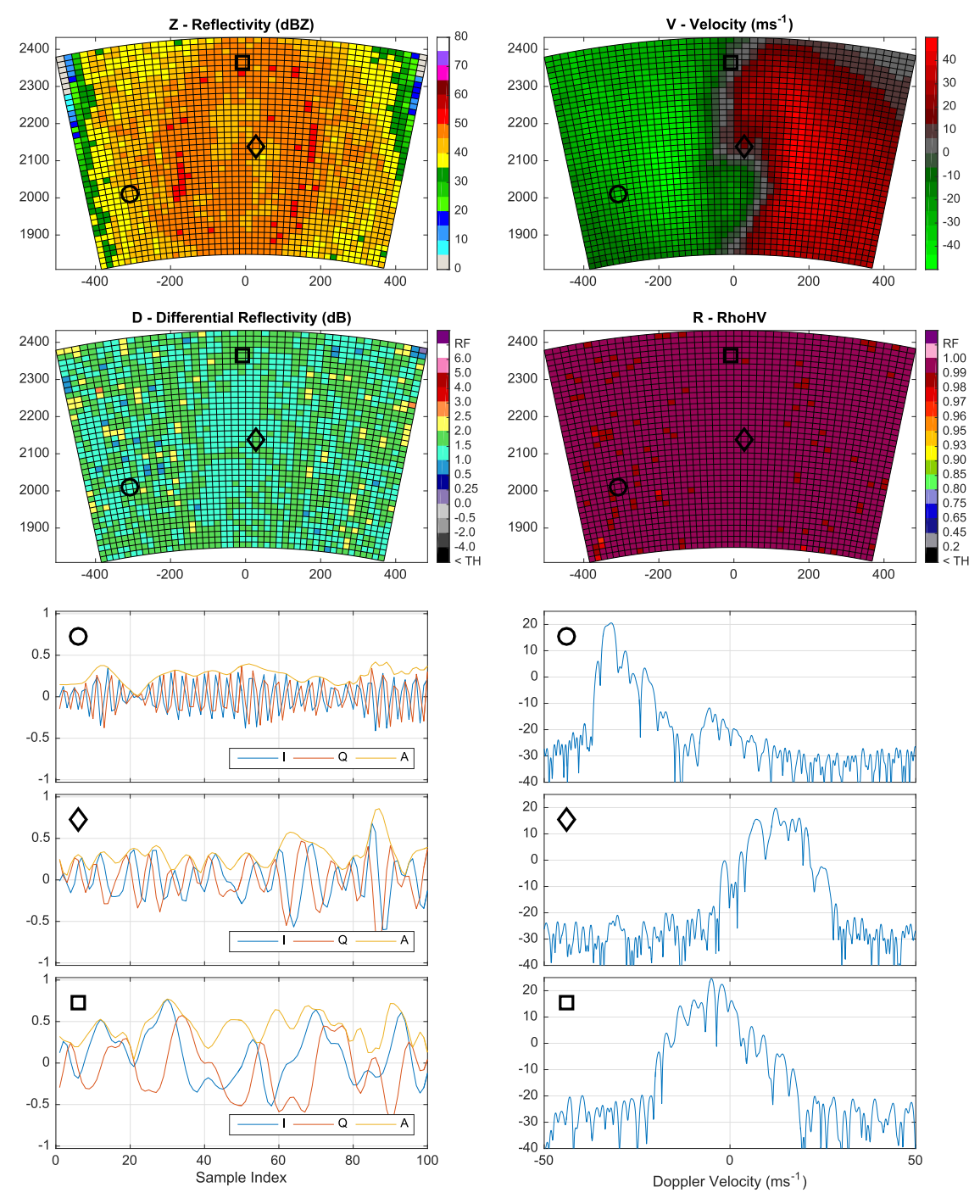


Fig. 10. Example PPI displays of radar variables and time-series data from a simulation with only meteorological scatterers. Three radar cells are highlighted, along with their time-series samples and spectra shown on the bottom panels. The radar cell identified by a circle  $(\bigcirc)$  is a canonical weatherlike example where velocity of the targets have a Gaussian distribution about the mean velocity. The radar cell identified by a diamond  $(\diamond)$  is at the center of the vortex, where the Dopler velocity is expected to be near zero. Finally, the radar cell identified by a square  $(\square)$  shows an example at the zero isodop region. These examples will be repeated with the presence of debris in the simulation domain.

It is noted here that debris objects are not affected by  $D_s$ . Each object is emulated independently as a point target. There is no scatterer density to parameterize this set of scatterers.

#### III. EXPERIMENTAL RESULTS

Two cases are presented to demonstrate the capability of the simulator. An experiment with only meteorological scatterers will first be presented, then followed by another with identical background configurations but with the addition of debris.

#### A. Meteorological Scatterers Only

An experiment with meteorological scatterers only was conducted using a simple MP DSD with only five discrete drop sizes, i.e., 1–5 mm. A tornadic vortex is placed at about 2 km away from the radar. After the time-series samples are collected, a standard spectral estimator is applied to derive the radar products.

Fig. 10 shows the radar products and time-series samples from the radar simulator. Four plan position indicators (PPI) of

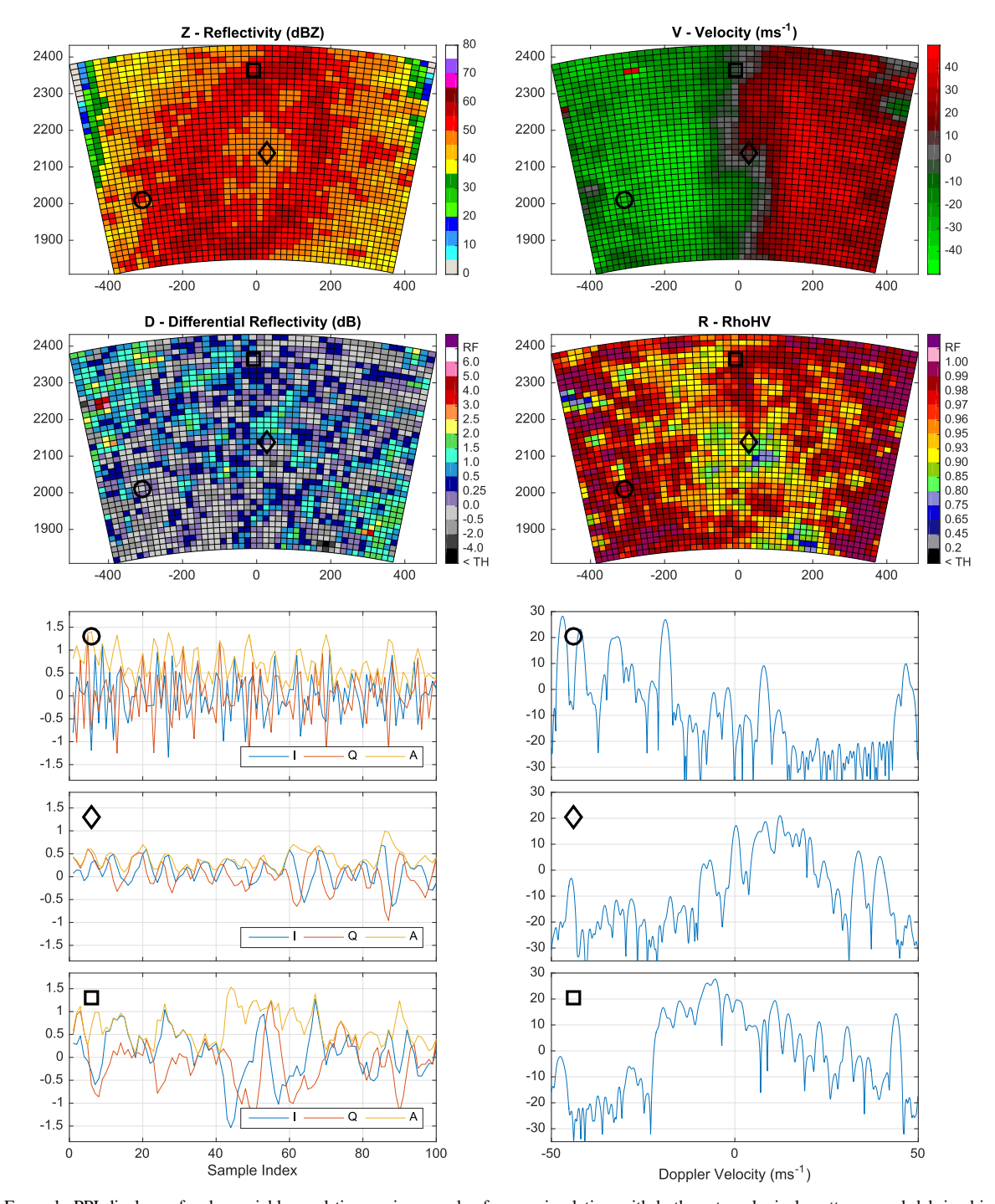


Fig. 11. Example PPI displays of radar variables and time-series samples from a simulation with both meteorological scatterers and debris objects. A wide region of negative  $Z_{DR}$  and low  $\rho_{HV}$  can readily be seen owing to the contributions from debris. The radar cell identified by a circle ( $\bigcirc$ ) now has a new signal component due to debris that is dragged and lifted from the surface. The radar cell identified by a diamond ( $\circ$ ) is almost the same as the previous setup as no debris are expected to be lifted at the areas with low wind velocity. Finally, the radar cell identified by a square ( $\square$ ) is the most complex of all. It contains many new signal components compared with the previous experiment, indicating a large number of debris objects being brought into this radar cell.

reflectivity in dBZ, velocity in m s<sup>-1</sup>, differential reflectivity in dB, and cross correlation coefficient are shown on the top. I/Q time-series samples and their corresponding spectra are shown on the bottom panels for three selected radar cells. These radar cells are highlighted for specific discussions in the following.

In general, scatterer centrifuging and size-sorting effects are apparent on the reflectivity map, with a ring of

higher reflectivity and a weak echo hole [35], [36] in the middle indicating the center of the vortex. Doppler velocity clearly shows the inbound and outbound components, just like a typical velocity couplet one would expect to see in a tornado. Differential reflectivity is positive, as all the scatterers are modeled as ellipsoids, and the cross-polar correlation coefficient is close to one, as expected.

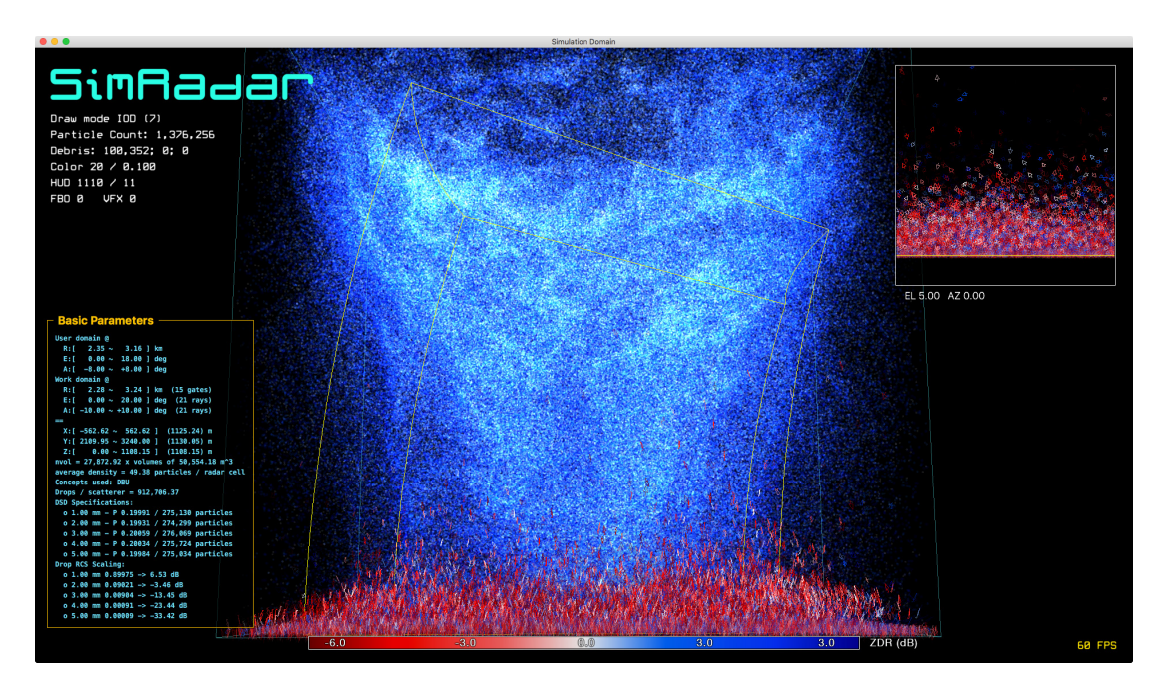


Fig. 12. GUI using a draw mode to color the scatterers based on their  $Z_{DR}$  and to assign their opacity based on their RCS amplitude. The majority of the meteorological scatterers are in blue region as expected. Compared with Fig. 6, a significant number of the debris objects have disappeared as most of them are not facing the radar. For the ones that do, their  $Z_{DR}$  values are negative.

The radar cell highlighted with a circle (()) represents a dwell at the outer fringe of a tornado vortex where the velocity is relatively uniform compared with elsewhere; this can be confirmed from the narrow signal spectrum. The radar cell highlighted with a diamond ( $\diamond$ ) shows one example signal that has a low Doppler velocity and wide spectrum width, which is what one would observe near the center of a tornado vortex. Finally, for the radar cell highlighted with a square (()), right in the zero isodop, the time-series data can be seen to exhibit a slow oscillation. Its spectrum is of a narrow Gaussian shape near zero velocity, as expected. Next, an identical simulation setup with the addition of debris particles is shown.

#### B. Debris

As mentioned in Section I, a major motivation of this paper is to investigate the hypothesis of common alignment of the tornadic debris. A simple experiment was conducted with approximately  $2\times 10^6$  leaves using the same meteorological background as in the previous example. The radar variables and time-series samples of this experiment are shown in Fig. 11. The TDS is similar to what is expected, i.e.,  $Z > 45\,\mathrm{dBZ}$ ), a velocity couplet and  $\rho_{HV} < 0.8$ .

As expected, radar reflectivity Z shows a slight increase in magnitude owing to the contributions from debris. The radial velocity measurement is overall similar to the previous example but more "noisy," which can be attributed to the less coherent interactions between signals from the debris and signals from the meteorological scatterers. A region of negative  $Z_{DR}$  can readily be seen. It also has lower  $\rho_{HV}$ , indicating where debris concentration is higher.

Recall that the radar cell highlighted with a circle (()) is at the outer fringe of the tornado vortex. Compared with the

previous setup, a new mode of signals at a lower Doppler velocity can be seen in the spectrum of this radar cell, indicating that most of the debris are at the onset of being lofted from the surface. Radar cell highlighted with a diamond ( $\diamond$ ) is virtually identical to the previous example, as no significant debris are expected in this area. For radar cell highlighted with square ( $\square$ ), many new signals can be seen in the spectrum, indicating significant effects due to the debris. This is also the area where  $Z_{DR}$  and  $\rho_{HV}$  are prominently negative and low, respectively.

Through the visualization tool, we are able to see that a majority of the debris objects with strong reflections (high RCS) are oriented vertically. Fig. 12 shows an identical scene to Fig. 6 but using a draw mode to color the scatterers using their  $Z_{DR}$  values, with red for negative values, blue for positive values, and opacity as a function of their reflectivity, i.e., scatterers with low RCS from the perspective of the radar are drawn to be transparent while scatterers with high RCS are drawn to be completely opaque. By comparing the two, one can readily see that a large portion of the debris disappeared, due to their transparent color as they are less reflective. Moreover, debris objects that have high reflectivity values are oriented facing the radar, as expected. It is evident that most are red, indicating negative  $Z_{DR}$ , which is equivalent to the vertical orientation. This experiment confirms the hypothesis that common debris alignment can happen. A separate work to investigate this phenomenon in detail is currently underway and will be documented in a future work.

## IV. CONCLUSION AND FUTURE WORK

A framework to synthesize polarimetric weather radar timeseries samples using physical hydrometeors and debris objects has been introduced. The framework utilizes tornadic wind fields produced by an LES model for the scatterer motions and orientations, using only electromagnetic approximations to produce radar simulations of a realistic TDSs, which is a region of negative  $Z_{DR}$  and low  $\rho_{HV}$ , indicating the presence of debris and common alignment.

We will continue to expand the ADM library and RCS library as we explore other scientific objectives. With this tool, there are several interesting science questions that can be answered readily, one of which is a detailed study of the debris orientation. As the unit quaternion of each debris objects is available, we could quantify the orientation through a statistical analysis to assess and characterize the orientation distributions.

In addition, there is a parallel effort to use signal processing methods to investigate the polarimetric signal spectra of the data. The results could potentially lead to new and unique scanning strategies or instrumentation designs to atmospheric scientists collect different kinds of observation for tornado studies.

While the tool presented here was primarily developed based on the study of tornadic debris, the ADM- and RCSbased polarimetric time-series simulation can be used beyond meteorological applications. One could potentially use this tool to explore nonmeteorological objects with complex RCS, such as chaff, birds, or insects.

#### ACKNOWLEDGMENT

This paper represents significant results from the collaborative effort between the Advanced Radar Research Center (ARRC) of the University of Oklahoma and the Disaster Prevention Research Institute at Kyoto University. The authors would like to thank the Collaborative Research Program of the Joint Usage/Collaborative Research Center for Multidisciplinary Disaster Prevention Study: DPRI Kyoto University. They would also like to thank A. Umeyama, J. Lujan, and Y. Zhu for their assistance throughout the project.

## REFERENCES

- [1] K. M. Simmons and D. Sutter, "WSR-88D radar, tornado warnings, and tornado casualties," Weather Forecast., vol. 20, pp. 301-310, Jun. 2005.
- D. S. Saxion et al., "New science for the WSR-88D: Validating the dual polarization upgrade," in Proc. 27th Conf. Interactive Inf. Process. Syst. (IIPS), Seattle, WA, USA, Jan. 2011, p. 365.
- [3] A. V. Ryzhkov, T. J. Schuur, D. W. Burgess, and D. S. Zrnič, "Polarimetric tornado detection," J. Appl. Meteorol., vol. 44, pp. 557-570,
- [4] C. J. Schultz et al., "Dual-polarization tornadic debris signatures part II: Comparisons and caveats," Electron. J. Oper. Meteorol., vol. 13, no. 9, pp. 120-137, Nov. 2012.
- [5] D. J. Bodine, M. R. Kumjian, R. D. Palmer, P. L. Heinselman, and A. V. Ryzhkov, "Tornado damage estimation using polarimetric radar," Weather Forecast., vol. 27, pp. 138-158, Feb. 2013.
- [6] A. V. Ryzhkov, S. E. Giagrande, V. M. Melnikov, and T. J. Schuur, "Calibration issues of dual-polarization radar measurements," J. Atmos. Ocean. Technol., vol. 22, pp. 1138-1155, Aug. 2005.
- [7] D. Bodine, R. D. Palmer, and G. Zhang, "Dual-wavelength analyses of tornadic debris signatures," J. Appl. Meteorol. Climatol., vol. 53, no. 2, pp. 242-261, Feb. 2014.
- [8] D. S. Zrnič, "Simulation of weatherlike Doppler spectra and signals," J. Appl. Meteorol., vol. 14, no. 4, pp. 619-620, Jun. 1975.
- [9] D. A. Holdsworth and I. M. Reid, "A simple model of atmospheric radar backscatter: Description and application to the full correlation analysis of spaced antenna data," Radio Sci., vol. 30, no. 4, pp. 1263-1280, Jul. 1995.

- [10] G. Galati and G. Pavan, "Computer simulation of weather radar signals," Simul. Pract. Theory, vol. 3, no. 1, pp. 17-44, Jul. 1995.
- [11] C. Capsoni and M. D'Amico, "A physically based radar simulator," J. Atmos. Ocean. Technol., vol. 15, no. 2, pp. 593-598, Apr. 1998.
- [12] C. Capsoni, M. D'Amico, and R. Nebuloni, "A multiparameter polarimetric radar simulator," J. Atmos. Ocean. Technol., vol. 18, no. 11, pp. 1799-1809, Nov. 2001.
- [13] B. L. Cheong, R. D. Palmer, and M. Xue, "A time series weather radar simulator based on high-resolution atmospheric models," J. Atmos. Ocean. Technol., vol. 25, no. 2, pp. 230-243, Feb. 2008.
- [14] L. Lei et al., "Multilag correlation estimators for polarimetric radar measurements in the presence of noise," J. Atmos. Ocean. Technol., vol. 29, no. 6, pp. 772-795, Jun. 2012.
- [15] A. D. Byrd et al., "A weather radar simulator for the evaluation of polarimetric phased array performance," IEEE Trans. Geosci. Remote Sens., vol. 54, no. 7, pp. 4178-4189, Jul. 2016.
- [16] L. Lei, G. Zhang, B. L. Cheong, R. D. Palmer, and M. Xue, "Simulations of polarimetric radar signals based on numerical weather prediction model output," in Proc. 25th Conf. IIPS Meteorol., Oceanogr., Hydrol., Phoenix, AZ, USA, 2009, pp. 1–6.
- M. Tachikawa, "Trajectories of flat plates in uniform flow with application to wind-generated missiles," J. Wind Eng. Ind. Aerodyn., vol. 14, pp. 443-453, Dec. 1983.
- [18] T. Uchida and Y. Ohya, "Large-eddy simulation of turbulent airflow over complex terrain," J. Wind Eng. Ind. Aerodyn., vol. 91, nos. 1-2, pp. 219-229, 1986.
- [19] T. Maruyama, "Simulation of flying debris using a numerically generated tornado-like vortex," J. Wind Eng. Ind. Aerodyn., vol. 99, no. 4, pp. 249-256, 2011.
- [20] D. J. Bodine, T. Maruyama, R. D. Palmer, C. J. Fulton, H. B. Bluestein, and D. C. Lewellen, "Sensitivity of tornado dynamics to soil debris loading," J. Atmos. Sci., vol. 73, no. 7, pp. 2783-2801, 2017.
- [21] P. J. Richards, "Dispersion of windborne debris," J. Wind Eng. Ind. Aerodyn., vols. 104–106, pp. 594–602, May 2012. [22] T. Maruyama and M. Noda, "Tornado-borne debris," J. Appl. Wind Eng.,
- vol. 37, pp. 124-129, 2012.
- [23] J. B. Kuipers, Quaternions and Rotation Sequences: A Primer With Applications to Orbits, Aerospace, and Virtual Reality. Princeton, NJ, USA: Princeton Univ. Press, 1999.
- [24] M. Mishcheko, "Calculation of the amplitude matrix for a nonspherical particle in a fixed orientation," Appl. Opt., vol. 39, no. 6, pp. 1026-1031, 2000.
- [25] J. R. Wait, "Scattering of a plane wave from a circular dielectric cylinder at oblique incidence," Can. J. Phys., vol. 33, no. 5, pp. 189-195, 1955.
- [26] T. B. A. Senior, K. Sarabandi, and F. T. Ulaby, "Measuring and modeling the backscattering cross section of a leaf," Radio Sci., vol. 22, no. 6, pp. 1109-1116, Nov. 1987.
- [27] D. C. Jenn, Radar and Laser Cross Section Engineering (AIAA Education), 2nd ed. Washington, DC, USA: AIAA, 2005.
- [28] A. S. Horton, C. J. Fulton, J. Ruyle, and K. Hatami, "Investigation of electrical properties of clay soil," in Proc. Allerton Antenna Symp., Sep. 2014.
- [29] J. S. Marshall and W. M. Palmer, "The distribution of raindrops with size," J. Meteorol., vol. 5, pp. 165-166, Aug. 1948.
- [30] C. W. Ulbrich, "Natural variations in the analytical form of raindrop size distribution," J. Climate Appl. Meteorol., vol. 22, pp. 1764-1775, Oct. 1983.
- [31] P. T. Willis, "Functional fits to some observed drop size distributions and parameterization of rain," J. Atmos. Sci., vol. 41, pp. 1648-1661, May 1984.
- X. Dou, W. Liu, P. Amayene, and J. Liu, "Optimization of the parameter of the raindrop size distribution in rain rate measurement by airborne radar," Quart. J. Appl. Meteorol., vol. 10, no. 3, pp. 293-298,
- [33] R. Uijlenhoet and D. S. Torres, "Measurement and parameterization of rainfall microstructure," J. Hydrol., vol. 328, pp. 1-7, Aug. 2006.
- A. Tokay, P. G. Bashor, E. Habib, and T. Kasparis, "Raindrop size distribution measurements in tropical cyclones," Monthly Weather Rev., vol. 136, pp. 1669–1685, May 2008.
- [35] J. Wurman and S. Gill, "Finescale radar observations of the dimmitt, Texas (2 June 1995), Tornado," Mon. Weather Rev., vol. 128, pp. 2135-2164, Jul. 2000.
- [36] D. C. Dowell, C. R. Alexander, J. M. Wurman, and L. J. Wicker, "Centrifuging of hydrometeors and debris in tornadoes: Radar-reflectivity patterns and wind-measurement errors," Mon. Weather Rev., vol. 133, pp. 1501-1524, Jun. 2005.



**Boon Leng Cheong** was born in Malaysia in 1976. He received the Ph.D. degree in electrical engineering from the University of NebraskaLincoln, Lincoln, NE, USA, in 2005, with a dissertation on adaptive beamforming to observe the atmospheric boundary layer using the turbulent eddy profiler.

He is currently a Research Scientist with the Advanced Radar Research Center and an Adjunct Associate Professor with the School of Electrical and Computer Engineering, The University of Oklahoma, Norman, OK, USA. His research interests

include software-defined radar design, array signal processing, real-time software architecture, parallel computing, and numerical radar simulations.



**David J. Bodine** received the B.S., M.S., and Ph.D. degrees in meteorology from The University of Oklahoma (OU), Norman, OK, USA, in 2007, 2009, and 2014, respectively. He also received the M.S. degree in electrical and computer engineering from OU in 2012.

He was a Post-Doctoral Fellow with the National Center for Atmospheric Research, Boulder, CO, USA. He is currently a Research Scientist with the Advanced Radar Research Center, OU. His research interests include phased array and dual-polarization

radar observations of severe thunderstorms and tornadoes, radar simulation studies, and fluid dynamic simulations of severe thunderstorms and tornadoes.



**Caleb J. Fulton** (S'05–M'11–SM'16) received the B.S. and Ph.D. degrees in ECE from Purdue University, West Lafayette, IN, USA, in 2006 and 2011, respectively.

He is currently an Assistant Professor in ECE with the Advanced Radar Research Center, The University of Oklahoma, Norman, OK, USA. His work focuses on antenna design, digital phased array calibration and compensation for transceiver errors, calibration for high quality polarimetric radar measurements, integration of low-complexity trans-

ceivers and high-power GaN devices, and advanced digital beamforming design considerations. He is currently involved in a number of digital phased array research and development efforts for a variety of applications.

Dr. Fulton received the Purdue University Eaton Alumni Award for Design Excellence in 2009 for his work on the Army Digital Array Radar Project. He also received the Meritorious Paper Award for a summary of these efforts at the 2010 Government Microcircuit Applications and Critical Technologies Conference. He received the 2015 DARPA Young Faculty Award for his ongoing digital phased array research. He is a member of the IEEE Antennas and Propagation, Aerospace and Electronic Systems, and Microwave Theory and Techniques Societies, and serves on the Education Committee of the latter.



**Sebastián M. Torres** (S'98–M'02–SM'07) received the B.S. degree from the National University of Mar del Plata, Mar del Plata, Argentina, in 1995, and the M.S. and Ph.D. degrees in electrical engineering from The University of Oklahoma, Norman, OK, USA, in 1997 and 2001, respectively.

In 1997, he joined the Cooperative Institute for Mesoscale Meteorological Studies, The University of Oklahoma, where he is currently the Assistant Director and a Senior Research Scientist with the National Severe Storms Laboratory (NSSL). He is

also the Leader of the Advanced Radar Techniques Group, NSSL, he conducts Research and Development of Innovative Signal Processing and Adaptive Sensing Techniques to improve the quality, coverage, accuracy, and timeliness of meteorological products from weather radars. He is involved in the exploration and demonstration of unique capabilities offered by multifunction phased-array radar for weather observations, and the transfer of technology to existing radar systems in government, public, and private organizations.

Dr. Torres has received the 2011 Department of Commence Gold Medal as a member of the Radar Research and Development Division at NSSL for scientific and engineering excellence in adapting military phased-array-radar technology to improve U.S. weather radar capabilities, and the 2003–2004 Office of Oceanic and Atmospheric Research Outstanding Scientific Paper Award. He holds and Adjunct Faculty position with the School of Electrical and Computer Engineering, and is a member of the Graduate Faculty and the Advanced Radar Research Center, The University of Oklahoma.



**Takashi Maruyama** was born in Japan in 1958. He received the B.E., M.E., and Ph.D. degrees in architecture engineering from Kyoto University, Kyoto, Japan, in 1982, 1984, and 1994, respectively.

In 1985, he joined the Disaster Prevention Research Institute, Kyoto University, as a Research Associate. In 1995, he was with the Institute of Fluid Mechanics, Karlsruhe Institute of Technology, Karlsruhe, Germany, as a Visiting Researcher. Since 1998, he has been with the Disaster Prevention Research Institute, Kyoto University, where he was

an Assistant Professor, became an Associate Professor in 2007, a Professor in 2012, and a Vice-Director in 2015. His research interests include wind engineering, wind resistant construction, and numerical fluid mechanics.

Dr. Maruyama is a Fellow of the Japan Association for Wind Engineering, a member of the Architectural Institute of Japan, the Japan Society of Fluid Mechanics. He was a recipient of the Award for Outstanding Young Researchers 1993, the Encouragement Prize of the AIJ in 1999, the Award for Outstanding Papers of the JAWE in 2010 for his research works on numerical simulation of wind flow over urban area.



**Robert D. Palmer** (S'86–M'89–SM'93–F'17) was born in Fort Benning, GA, USA, in 1962. He received the Ph.D. degree in electrical engineering from The University of Oklahoma (OU), Norman, OK, USA, in 1989.

From 1989 to 1991, he was a JSPS Post-Doctoral Fellow with the Radio Atmospheric Science Center, Kyoto University, Japan, where his major accomplishment was the development of novel interferometric radar techniques for studies of atmospheric turbulent layers. He was with the Physics and

Astronomy Department, Clemson University, Clemson, SC, USA. From 1993 to 2004, he was a Faculty Member with the Department of Electrical Engineering, University of Nebraska, Lincoln, NE, USA, where his interests broadened into areas, including wireless communications, remote sensing, and pedagogy. He was with OU as the Tommy C. Craighead Chair with the School of Meteorology in 2004, He established the interdisciplinary Advanced Radar Research Center (ARRC). He currently serves as the Executive Director of the ARRC and OU's Associate Vice President for Research. While at OU, his research interests have focused on the application of advanced radar signal processing techniques to observations of severe weather, particularly related to phased-array radars and other innovative system designs. He has authored widely in the area of radar remote sensing of the atmosphere, with an emphasis on generalized imaging problems, spatial filter design, and clutter mitigation using advanced array/signal processing techniques.

Dr. Palmer is a Fellow of the American Meteorological Society. He has been the recipient of several awards for both his teaching and research accomplishments.